Soil Dynamics and Earthquake Engineering 198 (2025) 109624

Contents lists available at ScienceDirect

Soil Dynamics and Earthquake Engineering

journal homepage: www.elsevier.com/locate/soildyn

Deterministic numerical analysis of excess pore water pressure induced by 2012 earthquake in Pieve di Cento (Italy)

Lucia Mele [a,*], Fausto Somma [b]

[a] University of Napoli Federico II, Department of Civil, Architectural and Environmental Engineering, Napoli, Italy
[b] Ministry of Infrastructure and Transport, General Directorate for Dams and Water Infrastructure, Rome, Italy

ARTICLE INFO

Keywords:
Soil liquefaction
Pieve di cento
Seismic site response analyses
Filter effect
Soil-structure interaction

ABSTRACT

A large area in the Po River Valley (northern Italy) experienced extensive liquefaction phenomena following the seismic event of 20 May 2012. Several indicators of liquefaction, including ground subsidence, lateral spreading, and the appearance of sand boils, were observed. A significant number of buildings were damaged, displaying signs of tilting or subsidence. A reliable estimate of the excess pore pressure induced by seismic shaking within the soil is crucial for predicting the behavior of the soil on a large scale and, consequently, the effects of the earthquake on the built environment. In this study, deterministic analyses of the excess pore water pressure generated during the 2012 Italian earthquake were conducted at the Pieve di Cento site. The analyses were carried out with varying levels of complexity, ranging from loosely coupled to fully coupled dynamic approaches. The strong agreement in terms of excess pore pressure ratio (r_u) suggests that, if properly calibrated, both loosely and fully coupled models can accurately predict earthquake-induced excess pore water pressure and, consequently, liquefaction-induced damage. Additional insights into the impact of soil-structure interaction on excess pore water pressure buildup were also provided. The results suggest that structural loading alters the effective stress state within the soil, which in turn may significantly influence the excess pore pressure ratio relative to free-field conditions.

1. Introduction

The response of saturated soil during strong seismic motion is governed by complex mechanisms, primarily involving hysteretic behavior and volumetric-distortional coupling. The latter causes volumetric strains in drained conditions or changes in pore pressure under undrained conditions. In loose, saturated sandy soil deposits, these conditions can lead to a significant reduction in soil stiffness and strength, potentially resulting in liquefaction. When liquefaction occurs, sandy soils behave like a fluid, which can cause severe damage to structures and infrastructure. Accurately predicting earthquake-induced pore pressure (Δu) is essential for understanding the response of soil deposits and the subsequent effects on the built environment. Estimating earthquake-induced excess pore water pressure requires the use of appropriate computer codes, and a thorough understanding and correct application of these tools are critical for ensuring reliable results. Given the high strain range that occurs during liquefaction, non-linear effective stress analyses should be employed. Within this context, two approaches are used to predict earthquake-induced pore water pressures.

1) a “loosely coupled” approach, which predicts pore pressures using relationships combined with constitutive models formulated in total stress (e.g., pore pressure prediction based on accumulated strains or stresses) [1],
2) a “fully coupled” approach, which uses a constitutive model formulated directly in effective stress to predict both the stress-strain response and pore pressure response of the soil. In particular, coupled approaches are based on time-domain effective stress analyses, where soil behaviour is described through advanced constitutive models and the evolution of pore water pressures stems from rigorous hydro-mechanical coupling or semi-empirical pore pressure generation models [2,3]. Many plasticity-based constitutive models fall into this latter category [1].

Needless to say, loosely coupled approaches are easier to manage and generally require less calibration parameters if compared to those of fully coupled approaches. In other words, loosely coupled approach could be preferred by practitioners while fully coupled approaches are mostly used by geotechnical researchers and consultants.

* Corresponding author.
E-mail address: lucia.mele@unina.it (L. Mele).

https://doi.org/10.1016/j.soildyn.2025.109624
Received 8 December 2024; Received in revised form 14 June 2025; Accepted 20 June 2025
0267-7261/© 2025 Elsevier Ltd. All rights are reserved, including those for text and data mining, AI training, and similar technologies.

In May 2012, Italy experienced a significant seismic sequence. The main shock occurred on May 20, 2012 ($M_w = 6.1$), triggering extensive liquefaction (soil effective stresses approach to zero). The Po Valley, located in the foreland basin between the Alps and the northern Apennines in the Emilia-Romagna Region (Northern Italy), was particularly affected by the intense shaking [4]. The epicenter of this event (44.89°N latitude and 11.23°E longitude) was situated between the provinces of Modena and Ferrara, with the hypocenter at a depth of 6.3 km, classifying it as a shallow earthquake [5]. This earthquake holds significant interest in Italian seismic literature for several reasons: the extraordinary impacts it caused, the large area where liquefaction effects were observed, the extent of the damage, and the rarity of soil liquefaction cases in Italy [6,7]. Although Italy is a seismically active country, liquefaction typically occurs only in limited areas, resulting in generally localized damage.

The most pronounced liquefaction effects following the 2012 earthquake were observed in San Carlo (Municipality of Sant'Agostino) and Mirabello [5,7–9], where the subsoil consists of alluvial deposits with alternating layers of silty-clayey deposits and sandy soils. For example, photos in Fig. 1 (adapted from Ref. [7]) illustrate typical liquefaction effects, including sand boils, sinkholes, craters, surface ruptures, and extensional fissures. Many open spaces, such as courtyards, gardens, and roads, were completely covered by ejected sand, mud, and water. Also, in some areas such as the village of Scortichino located on the verge of a channel named "Canale Diversivo", quite close (less than 10 km) to the epicentre of the earthquake of the 20th of May, typical cracks and fissures on the ground generated by the lateral spreading phenomenon occurred. Numerous buildings were damaged [10,11], and 27 victims were recorded. In particular, Di Ludovico et al. [11], collected data about 1000 private residential masonry buildings located in several municipalities struck by the 2012 Emilia earthquake, differentiating structures with damages resulting from soil liquefaction from those affected by inertial seismic forces only. As a matter of fact, typical damages scenario derived by soil liquefaction are related to rigid building rotations, with a relevant loss of functionality of the structure while, in case of no liquefaction, out of plane mechanism or in plane diagonal cracks are commonly detected. It is fair to point out that, in case of no immediately activated soil liquefaction, the typical damage patterns can be mixed together.

An extensive study, including both in-situ and laboratory investigations, was conducted across a large area of the Po Valley [12–16] to geotechnically characterize the earthquake-affected region.

The objective of this paper is to conduct a deterministic numerical back-analysis of the excess pore water pressure induced by the 2012 earthquake at a reference site located in Pieve di Cento. Using various experimental data, dynamic effective stress analyses were performed employing both loosely coupled and fully coupled approaches, followed by a comparison of the results. In this context, the reliability of the loosely coupled approach, appropriately calibrated, was evaluated. Additionally, the seismic performance of a prototype building with a disconnected and continuous (raft) foundations, modeled as a masonry two-frame, two-bay structure, was investigated. Numerical modeling incorporating soil-structure interaction was employed to assess the differences in excess pore water pressure evaluation under free-field and non-free-field conditions.

The case study and the experimental investigations are briefly recalled in Section 2, where particular attention will be paid to the reference input motion used in numerical non-linear analyses, described

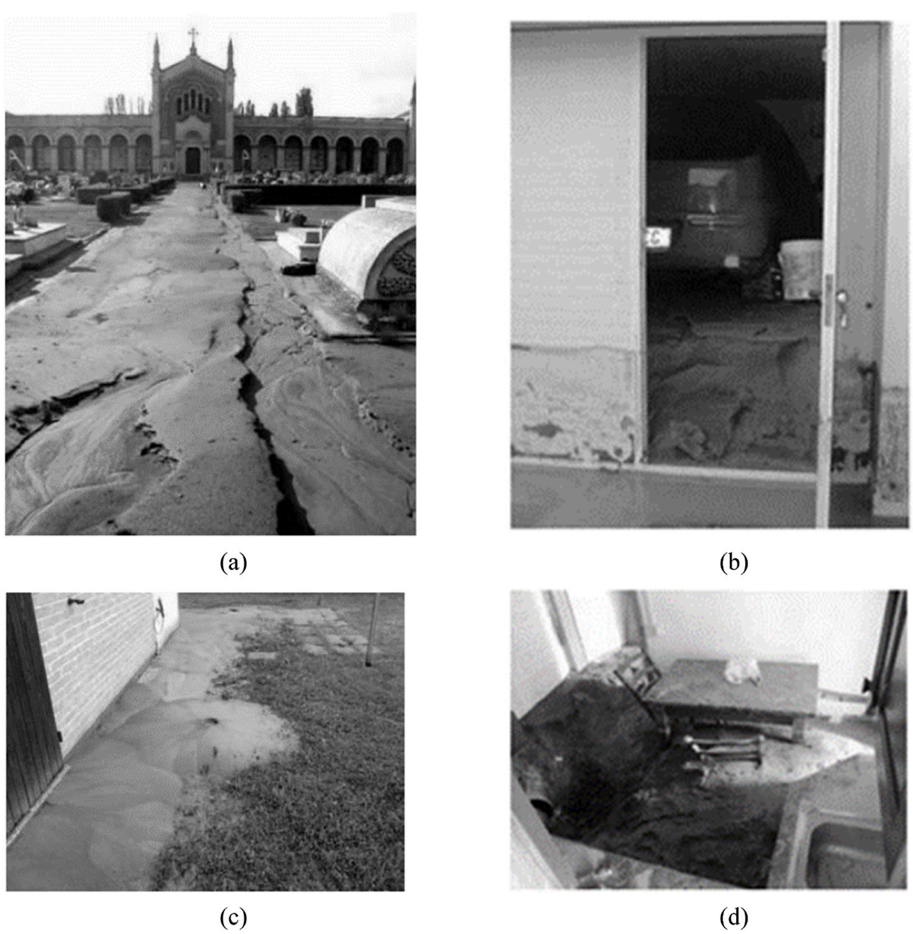

Fig. 1. Liquefaction evidence at San Carlo: main roads covered by grey silty sand ejected from the ground in San Carlo (a); garage (b); sand boils (c) and a private house (d) (adapted from Ref. [7]).

in sections 3 (1D analyses) and section 4 (2D analyses). Lastly, a summary of the main results will be reported in section 5.

2. The case study of Pieve di Cento (Italy)

As part of the European research project LIQUEFACT (http://www.liquefact.eu/), a reference site (44° 46’ 32.74" N; 11° 22’ 31.41" E) in the countryside near Pieve di Cento (at the boundary between the provinces of Bologna and Ferrara) was selected as a trial field to evaluate the effectiveness of various liquefaction mitigation measures (Fig. 2a–b) [16]. Pieve di Cento experienced widespread liquefaction following the mainshock of the 2012 seismic sequence (Fig. 2c–d). Specifically, as shown in Fig. 2e, at the selected reference point, numerous field observations of liquefaction (represented by red dots) were recorded. The

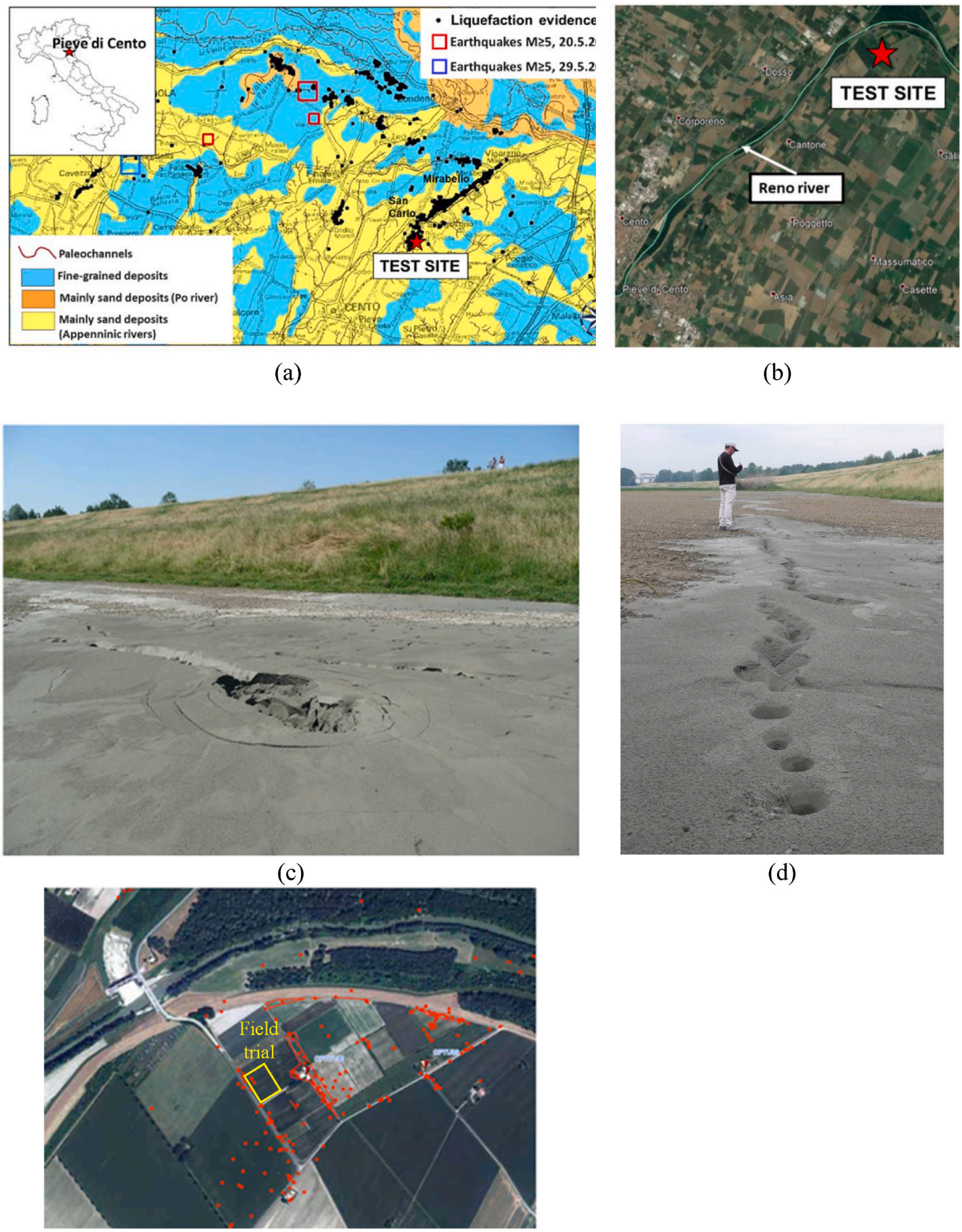

Fig. 2. (a) Location of the test site with in black liquefaction evidences after 2012 Emilia EQ [17]; (b) proximity to the Reno river [16]; (c–d) liquefaction evidences in Pieve di Cento [18]; (e) Map of the liquefaction points (red dots) detected in the bend of the Reno River in Pieve di Cento (modified from Ref. [19]).

available surveys indicated the presence of sandy and sandy-silt layers extending to a depth of 6–7 m.

In situ and laboratory tests were conducted to characterize the site. The geotechnical model is described in the following section.

2.1. Geotechnical model

A comprehensive in situ investigation was initially conducted to determine the stratigraphy column and mechanical behavior of the soils. Since liquefaction is a local phenomenon that typically affects the shallowest soil layers, the field investigation was limited to a depth of 10 m from the ground surface. However, given the considerable depth of the seismic bedrock roof (230 m below ground level, according to Minarelli et al., [13]), a deep soil model was required for the seismic response analysis of the site. This model was developed by integrating previous in situ investigations with geological study results [17,20].

The soil column is composed of alternating silty-clay and sandy soil deposits, divided into several geological units, called *subsystem* [20]. Shear wave velocity and thickness were assigned to each subsystem based on the data from Minarelli et al. [13] and geological sections obtained from the studies (Fig. 3a).

Fig. 3b highlights the shallow layering and the shear wave velocity profile as determined from a borehole and a Cross-Hole test conducted at the site. The representative soil column consists of an upper crust of silty sand approximately 0.8 m thick, followed by a silty sand layer extending to about 2.8 m depth. Beneath this is a grey silty sand deposit ranging from 2.8 to 6 m depth. A thin clayey layer is present within the silty sand deposits between 4.4 and 4.8 m depth, with similar formations continuing beyond 6 m depth. The upper silty sand layer ($1 < z < 2.8$ m) is characterized by a brownish color, referred to as Brown Silty Sand (BSS), while the deeper layer ($2.8 < z < 6.0$ m) has a greyish color and is named Grey Silty Sand (GSS). The groundwater table is located 1.8 m below the ground surface.

The ground investigation was complemented by comprehensive laboratory testing, including monotonic and cyclic triaxial tests, oedometer tests, and cyclic simple and torsional shear tests, conducted on both reconstituted and undisturbed specimens. The undisturbed samples were retrieved using Gel-Pusher [21,22] and Osterberg samplers.

Fig. 4 presents the grain size distribution curves for the liquefiable soils, Brown Silty Sand (BSS) and Grey Silty Sand (GSS). Table 1 provides a summary of their physical properties.

The liquefaction behavior of both BSS and GSS was investigated using cyclic triaxial (CTX) and cyclic simple shear (CSS) tests on specimens reconstituted in loose conditions (Dr ≈ 45 %). It is important to note that the cyclic simple shear tests were conducted using a non-conventional simple shear device equipped with flexible boundaries (latex membrane). The K_0 condition was simulated through a sophisticated control system: the horizontal stress (cell pressure) is imposed by operator through a linear-time function and the vertical piston moves in order to regulate axial strain (ε_a) in accordance with the volumetric strain (ε_v) evolution to maintain the condition $d\varepsilon_V/d\varepsilon_a = 1.0$ (i.e. $\varepsilon_r = 0$) and, therefore, the diameter constant. As a consequence, vertical stress changes in response to soil behaviour. During the cyclic phase the height of the specimen is kept constant. Since the height and volume are both

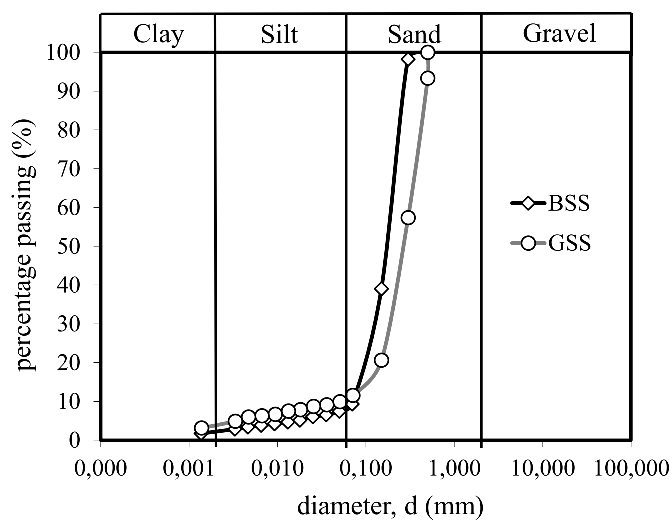

Fig. 4. Grain size distribution curve of Pieve di Cento sands.

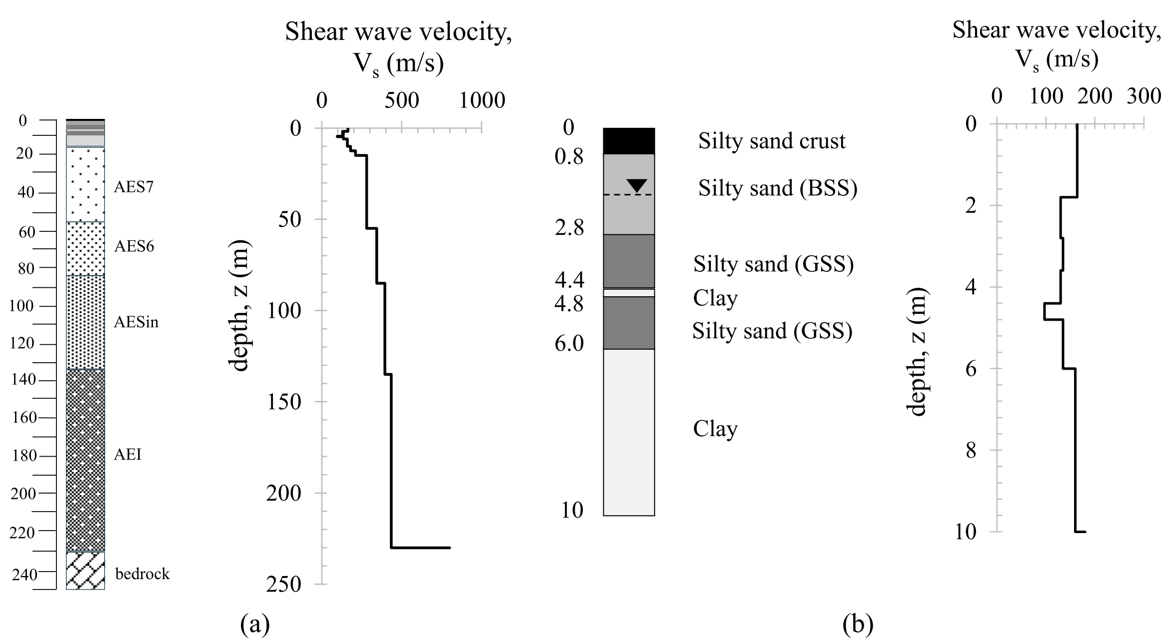

Fig. 3. (a) Pieve di Cento stratigraphy and Vs profile until bedrock and (b) zoom in shallowest layers.
Legend for Fig. 3a: Villa Verucchio Subsynthem (AES7); Bazzano Subsynthem (AES6); Undifferentiated Emiliano-Romagnolo Upper Synthem (AESin); Emiliano Romagnolo Lower Synthem (AEI), details in Paolucci et al., [20].

Table 1
Physical properties of Pieve di Cento liquefiable sands.

Soil	G_s	e_{max}-e_{min} [a]	D_{50} (mm)	FC (d < 0.075 mm) (%)	k_w (m/s) [b]	Ip (%)
BSS	2.667	1.04–0.546	0.18	8	$1.0 \cdot 10^{-4}$	–
GSS	2.655	0.884–0.442	0.30	11	$1.8 \cdot 10^{-5}$	–
Clay	2.699	–	–	–	–	30

[a] ASTM D4253-06 [23]; ASTM D4254-06 [24].
[b] estimated by laboratory permeability tests.

constant (undrained tests), the cross-sectional area does not change, as well. It allows to preserve simple shear conditions during the whole testing duration (further details in Mele, [25]).

The results of the cyclic tests have been plotted together on the N_{liq}–CRR plane. Here, N_{liq} represents the number of cycles (N_{cyc}) required to reach liquefaction for a given cyclic stress ratio (CSR), defined as $q/(2\cdot\sigma'_{c0})$ in CTX and τ/σ'_{v0} in CSS, where q is the cyclic deviatoric stress, τ is the cyclic shear stress, σ'_{c0} is the initial effective confining stress, and σ'_{v0} is the initial effective vertical stress. In the tests conducted, both σ'_{c0} and σ'_{v0} were set at 50 kPa.

To compare the results of cyclic triaxial (CTX) and cyclic simple shear (CSS) tests, the correlation proposed by Castro [26] can be utilized. Castro [26] introduced a correction factor (c_r) to account for the different stress paths in the two test types. According to his proposal, the cyclic resistance ratio (CRR) in cyclic triaxial tests (CRR_{ctx}) and cyclic simple shear tests (CRR_{css}) are related by the following equation:

$$CRR_{css} = c_r \cdot CRR_{ctx} \tag{1}$$

The correction factor (c_r) is determined by the coefficient of earth pressure at rest, K_0, using the equation:

$$c_r = \frac{2\cdot(1+2\cdot K_0)}{3\sqrt{3}} \tag{2}$$

The K_0 values, estimated from consolidation simple shear tests, are 0.479 for BSS and 0.490 for GSS [25]. Liquefaction was identified based on the stress criterion ($r_u = \Delta u/\sigma'_{v0} = 0.90$). Fig. 5a illustrates that a unique cyclic resistance curve (CRR-N_{liq}) can be identified for both BSS and GSS.

Additionally, a torsional shear test was conducted on an undisturbed specimen of GSS ($e_0 = 0.778$). The results of this test are presented in Fig. 5b on the γ–G/G_0–D plane, where γ is the shear strain, G is the shear modulus, G_0 is the shear modulus at small strains, and D is the damping ratio.

2.2. Reference input motion

The main shock of the Emilia 2012 earthquake sequence, which occurred on May 20, 2012, was recorded by the MRN station of the Italian strong-motion network (RAN), located on Napoli Street in Mirandola. However, this record cannot be directly used as a reference input motion for seismic response analysis because the station is situated on deep soft subsoil with an equivalent shear wave velocity ($V_{s,30}$) of 208 m/s, classifying it as a Class C site according to Eurocode 8 (EC8) [27]. Therefore, it is necessary to deconvolve the acceleration record from the MRN station to the bedrock level.

The deconvolution process requires a defined subsoil model beneath the recording station. Fig. 6a illustrates the stratigraphic profile, which consists of alternating layers of silt (B), sand (A200, A400), and clay (C). At a significant depth, these alternating sand and clay layers have been modeled as a single material (AL) [28]. The Vs-profile obtained from Cross-hole tests is also shown in Fig. 6b.

As noted by Chiaradonna et al. [28], since no site-specific laboratory data were available, the shear modulus reduction and damping curves (Fig. 6d) were assumed to be the same as those derived from cyclic and dynamic laboratory tests on soil samples taken from Scortichino, located 25 km from the MRN station [12].

The recorded input motion was downloaded from the ITACA database (https://itaca.mi.ingv.it/ItacaNet_40/#/home) and is shown in Fig. 6c (PGA = 0.262g). The seismic signal recorded at the ground surface was band-pass filtered using a second-order Butterworth filter, with a low-frequency cutoff of 0.04 Hz and a high-frequency cutoff of 40 Hz, in order to remove low-frequency trends and high-frequency noise. The outcrop signal was deconvolved using the DEEPSOIL software [29], and the resulting accelerogram at bedrock (modeled as an elastic half space) is presented in Fig. 6e (PGA = 0.147g). Deconvolution was performed with a 1D equivalent linear frequency domain analyses with a visco-elastic approach. All relevant information concerning both the recorded ground motion and the deconvolved seismic input at the bedrock level is provided in Table 2.

Although ground motion attenuation effects should be considered, Pieve di Cento and MRN station share the same Joyner-Boore distance (R_{JB}). Therefore, the expected PGA at both sites should be similar, and no scaling factor was applied to transfer the ground motion from MRN station to Pieve di Cento [16]. In other words, the signal shown in Fig. 6e was used as the outcrop reference motion for the Pieve di Cento site Fig. 3a.

Using a well-calibrated non-linear constitutive model based on effective stresses would be sufficiently accurate for modeling the dynamic response of the soil profile. However, this approach requires extensive in-situ and laboratory testing on the geotechnical layers, which is not available. Consequently, instead of performing a detailed effective-stress analysis for the entire profile, the focus was on the uppermost 10 m, for which more data were accessible.

To derive the within ground motion at Pieve di Cento at 10 m depth, which is crucial for analyzing thoroughly the dynamic response of the shallow soil profile shown in Fig. 3b, the deconvolved motion (Fig. 6e) was propagated from the assumed bedrock (230 m deep) up to the surface (Fig. 3a) using visco-elastic equivalent analysis implemented in

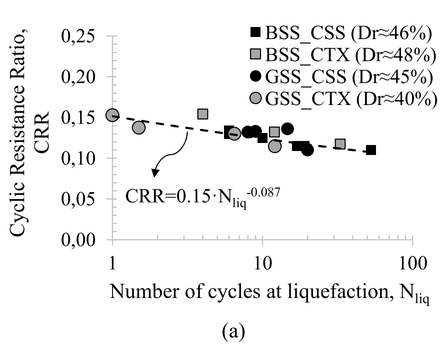

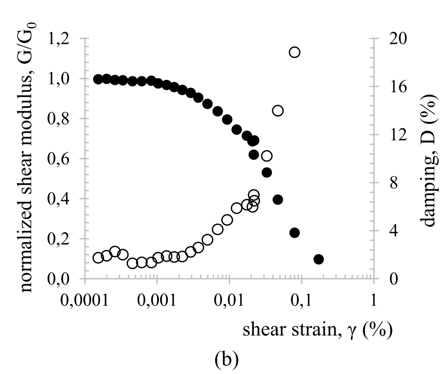

Fig. 5. (a) Cyclic resistance curve of both BSS and GSS sands and (b) decay curve of GSS sand (adapted from Flora et al., [16]).

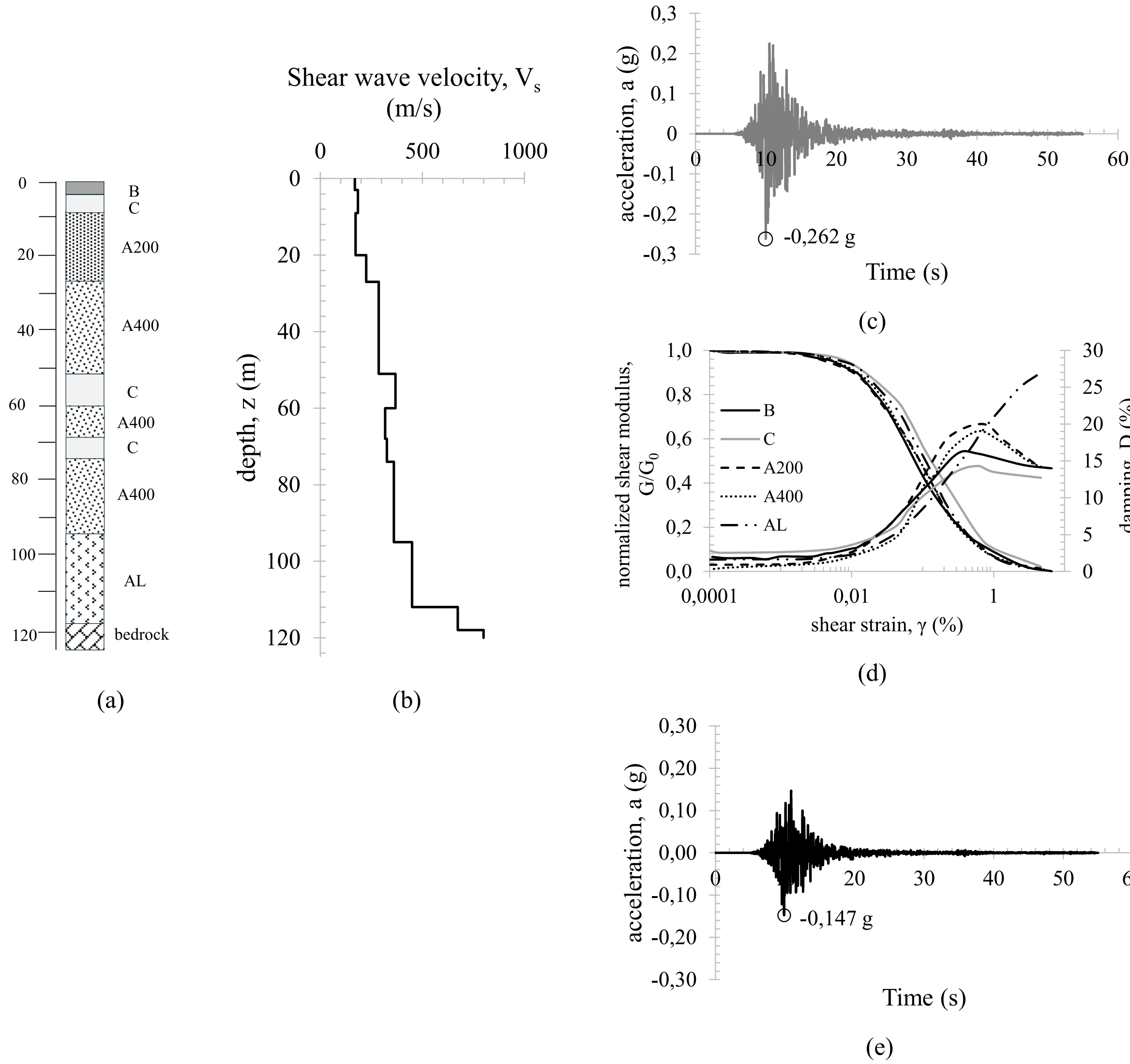

Fig. 6. (a) Stratigraphy profile at MRN station, (b) Vs – profile from Cross-Hole test; (c) EW acceleration time history, (d) normalized shear modulus and damping curves and (e) deconvolved motion in terms of acceleration time history.

Table 2
Mirandola and Pieve di Cento ground motion properties.

Parameter	Mirandola surface outcrop	Mirandola equivalent bedrock	Pieve di Cento (10m) within
$\|a_{max}\|$ (g)	0.262	0.147	0.150
f_d (Hz)	3.12	3.57	2.50
f_m (Hz)	2.19	2.44	1.24
I_A (m/s)	0.715	0.232	0.198
$T_{5\text{-}95}$ (s)	5.53	5.76	5.22

a_{max} = maximum acceleration; a_{min} = minimum acceleration; f_d = predominat frequency; f_m = medium frequency; I_A= Arias intensity; $T_{5\text{-}95}$ = significant duration.

the DEEPSOIL code.

For modeling the non-linear and dissipative behavior of soils, the curves in Fig. 5b were applied to the GSS and BSS layers. For the clay formations, experimental curves from Scortichino deposits were used (corresponding to C in Fig. 6d). For deeper layers (greater than 10 m), dynamic material curves were generated using the Darendeli [30] curves, with a plasticity index of 30 % and an OCR of 1 [31]. Fig. 3a displays the soil layering and the Vs profile based on all available information [31].

The within ground motion obtained at 10 m is presented in Fig. 7, including the acceleration time history (Fig. 7a) and the corresponding acceleration response spectrum (Fig. 7b). The main properties are reported in Table 2.

3. 1D Non-linear dynamic analyses

This section presents the results of 1D non-linear analyses used to estimate pore water pressures generated during the 2012 mainshock seismic sequence at the Pieve di Cento site. The findings from effective stress analyses conducted using both loosely coupled and fully coupled approaches will be discussed in Sections 3.1 and 3.2, respectively.

3.1. Deepsoil analyses

In addition to visco-equivalent total stresses analysis, DEEPSOIL code allows to perform effective stress analyses according to a loosely coupled approach. It offers a range of simplified pore water pressure models [32]. Among these, energy-based excess pore water pressure models were considered, since they result both simple and effective for estimating earthquake-induced pore water pressures.

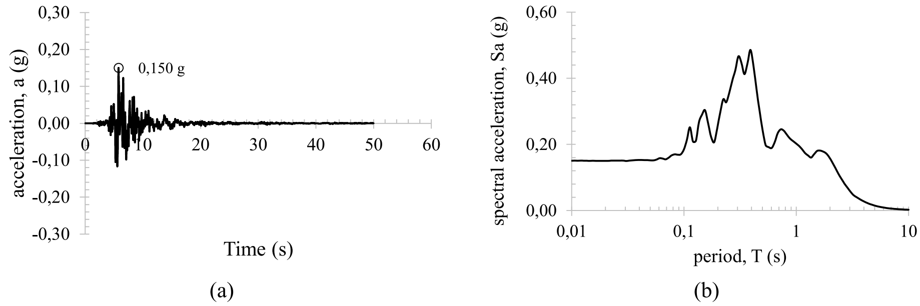

Fig. 7. (a) Acceleration time history at 10 m from ground surface and (b) acceleration response spectrum.

3.1.1. *Energy based pore pressure generation models*

Unlike traditional stress and strain pore pressure models, which often require complex and sometimes unreliable conversions of earthquake shaking into an equivalent number of uniform shear stress cycles [33, 34], energy-based models offer a more straightforward approach. These models (e.g., Refs. [35–37]) link pore pressure generation to the energy dissipated per unit volume of soil, or specific deviatoric energy (E_s). This approach provides a more comprehensive assessment of the cyclic stress-strain behavior of soils. Specifically, the specific deviatoric energy ($E_{s,i}$) for a given load cycle i (N_i) is calculated as the sum of the areas enclosed by stress-strain hysteresis loops (Fig. 8, [38]). For cyclic triaxial tests, this is expressed by Equation (3a):

$$E_{s,i} = \sum_{N_{cyc}=1}^{N_{cyc}=N_i} \iint_{D_{cyc}} dq \cdot d\varepsilon_s \tag{3a}$$

where q is the deviatoric stress and ε_s is the distorsional strain defined as $2/3(\varepsilon_a\text{-}\varepsilon_r)$, where ε_a and ε_r are axial and radial strains, respectively; and through Eq. (3b) for cyclic simple shear tests:

$$E_{s,i} = \sum_{N_{cyc}=1}^{N_{cyc}=N_i} \iint_{D_{cyc}} d\tau \cdot d\gamma \tag{3b}$$

where τ and γ are shear stress and strain, respectively.

In this paper the simple model proposed by Berrill & Davis [35] has been used. They introduced the following empirical formulation, which is implemented in DEEPSOIL:

$$r_u = \alpha \cdot W_s^{\beta} \tag{4}$$

where W_s represents the energy dissipated per unit volume of the soil normalized to the initial mean effective stress ($W_s = E_s/\sigma'_0$), and α and β are parameters to be calibrated through cyclic laboratory tests. Mele et al., [39] proposed a straightforward calibration method using in-situ CPT or SPT test results. In this research as suggested by Berrill & Davis

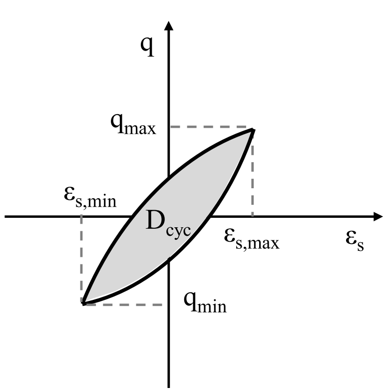

Fig. 8. Cycle in q-ε_s plane to evaluate specific deviatoric energy from cyclic triaxial tests (D_{cyc} is the area of a cycle) [38].

[35], β, has been assumed constant and equal to 0.50, while α can be related to the equivalent corrected CPT tip resistance (q_{c1Ncs}) or the corrected SPT blowcount ($(N_1)_{60cs}$) through the following relationships:

$$\alpha = 0.75 \cdot exp[5.29 \cdot (-0.073 \cdot ln(q_{c1Ncs}) + 0.74)] \tag{5a}$$

$$\alpha = 0.75 \cdot exp[5.29 \cdot (-0.046 \cdot ln((N_1)_{60cs}) + 0.52)] \tag{5b}$$

3.1.2. *Results of analysis*

Effective stress analysis using DEEPSOIL was conducted with the pore pressure generation model proposed by Berrill & Davis [35] for silty sands, with parameters α and β calibrated using the procedure outlined by Mele et al. [39]. The equivalent corrected CPT tip resistance q_{c1Ncs} was derived from the results of five in-situ CPT tests (Fig. 9a) using the correlations proposed by Boulanger & Idriss [40]. Subsequently, the values α Eq. (5a) were calculated (Fig. 9b).

Input motion (Fig. 7a) was applied as an inside motion at the base of the reference soil column (depth z = 10 m, Fig. 3b).

Fig. 10a shows $r_{u,max}$ profile of Pieve di Cento site. The analysis results indicate that liquefaction occurs in the GSS layers (approximately 4 and 5 m deep), which aligns with in-situ observations from the 2012 earthquake (e.g., Ref. [7]). Thus, despite its simplicity, the model seems to effectively predict the observed liquefaction.

The observation that liquefaction is more prominently triggered in the deeper portion of the GSS layer (4.8–6.0 m) compared to the shallower section (1.8–4.4 m) may be attributed to the so-called *filter effect*. This phenomenon implies that, once a deeper layer undergoes liquefaction, it acts as a damper, attenuating the upward propagation and amplification of the seismic waves. Consequently, lower $r_{u,max}$ values

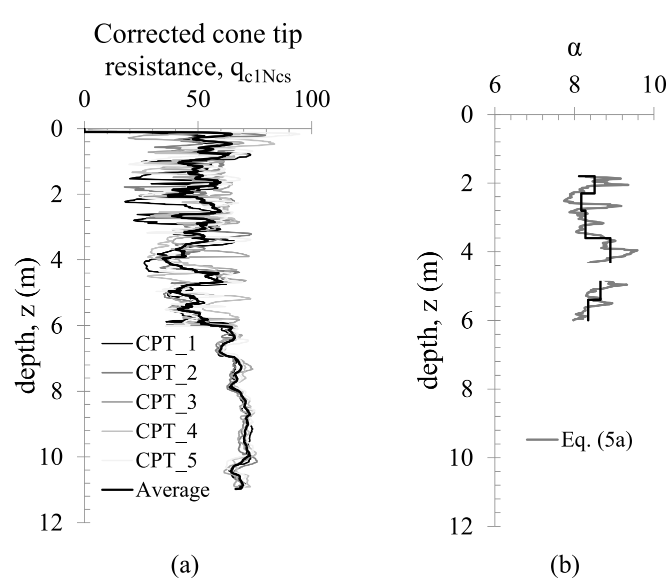

Fig. 9. (a) q_{c1Ncs} profile and (b) α calibration.

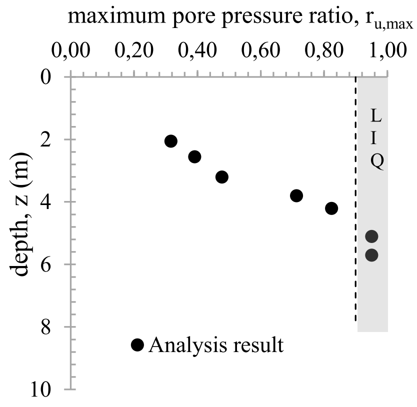

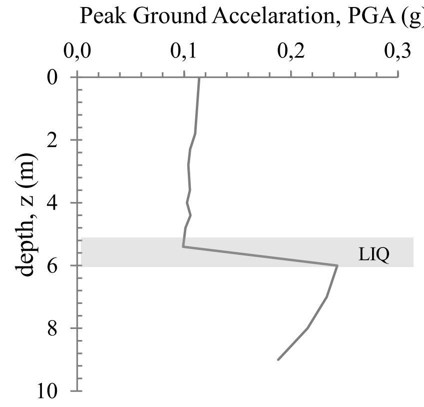

Fig. 10. (a) Estimated $r_{u,max}$ profile of Pieve di Cento site during the 2012 mainshock seismic sequence; (b) Estimated PGA profile.

are observed in the shallower layers. This effect is particularly evident when examining the peak ground acceleration (PGA) profile presented in Fig. 10b, which is derived by extracting, for each depth, the maximum absolute value of acceleration from the computed time history at that depth. As can be observed, a significant reduction in peak accelerations occurs in the zones where liquefaction develops. Parametric analyses conducted with DEEPSOIL (not shown here for brevity), using accelerograms scaled by different factors, indicate that the filter effect diminishes as the input motion is reduced. Specifically, when the accelerogram is scaled by a factor of 0.7 (PGA = 0.105g), a noticeable reduction in the filter effect is observed. Under more extreme conditions—such as scaling by a factor of 0.3 (PGA = 0.045g) —the filter effect disappears entirely due to the very limited generation of excess pore water pressure.

3.2. Analysis with advanced constitutive models

To compare the estimated pore pressure achieved with a loosely coupled approach, analysis by using advanced constitutive models (*fully coupled* approach) have been used. Analysis has been performed with PLAXIS, a commercial 2D Finite Element program, which can perform dynamic analyses by adopting several constitutive models. In this research two advanced constitutive models have been used: PM4Sand for liquefiable soils (sands in Fig. 3b) and Hardening Soil small strain (HS_{ss}) for the clayey layers, upper crust of silty sand and soil above the ground water table (first 1.8 m in Fig. 3b). Similar to the DEEPSOIL analysis, the 1D non-linear analysis conducted with PLAXIS were performed applying the within input motion (Fig. 7a) at a depth of 10 m. As reported by Kwok et al. [41], rigid base boundary must be used in combination with inside motion.

PM4Sand model [42] is a constitutive model which is able to simulate successfully the undrained behaviour of sands during earthquake loading, including the generation of pore pressures and liquefaction phenomena. PM4Sand is a stress ratio controlled bounding surface model, based on the plasticity model initially developed by Dafalias and Manzari [43], that incorporates the state-dependent soil behaviour through the compliance of the model with critical state considerations. It is developed to analyze the triggering of liquefaction and the resulting deformations in the soil for plane strain conditions. Originally, the bounding surface plasticity framework comprises two yield surfaces with the inner one enclosing the elastic region and the outer one functioning similar to the conventional yield surface. Plastic strains can be simulated when the loading causes the stress state to lie between these two surfaces and unloading is fully elastic. The PM4Sand model uses additional loading surfaces such as critical state surface and dilatancy surfaces. Moreover, it is cast in terms of the relative state parameter (ξ_R), which measures the difference between the relative density (D_r) and the relative density at critical state (D_{rcs}) for the current confining pressure [44]. This formulation allows soil properties to change during the simulation as a function of the change in state (i.e., changes in mean effective stress and/or in void ratio).

In this model there are 12 parameters to be calibrated, which are divided into two groups: the primary and secondary parameters. The primary parameters include: the apparent relative density (D_{r0}), the shear modulus coefficient (G_0) and the contraction rate parameter (h_{p0}). The secondary parameters include: atmospheric pressure (P_a), maximum and minimum void ratios (e_{max}, e_{min}), bounding surface parameter (n_b), dilatancy surface parameter (n_d), friction angle (φ_{cv}), Poisson's ratio (ν) and critical state Bolton's parameters (Q and R, Bolton, [45]). It should be specified that the bounding surface parameter (n_b) controls the rate of the bounding surface approaches the critical state surface and dilatancy. On the other hand, the dilatancy surface parameter (n_d) controls the stress-ratio at which contraction transitions to dilation, which is often referred to the phase transformation.

The primary parameters are required as model inputs, while the other 9 (P_a, e_{max}, e_{min}, n_b, n_d, φ_{cv}, ν, Q, R) can be left with their preset default values if no other information is available or calibrated to the desired response based on the available lab data.

The Hardening Soil model [46] is a nonlinear elasto-plastic material model. The failure in shear occurs according to Mohr-Coulomb criterion. In contrast to an elastic perfectly-plastic model, the yield surface of a hardening plasticity model is not fixed in principal stress space, but it can expand due to plastic straining. The Hardening Soil model with small strain stiffness (HS_{ss}) is a modification of the HS model that accounts for increased stiffness of soils at small strains. Also, the HS_{ss} can reproduce the soil hysteretic elastic behavior, and then, it can be applied to a certain extent for cycling loading as long as the cyclic mobility and the earthquake-induced pore water pressure is not crucial for a given application. This is due to the fact that, in unloading/reloading cycles, the numerical HS_{ss} behavior of soil is purely elastic and no accumulations of pore pressure, due to plastic strain accumulation, are developed. HS_{ss} model presents 15 parameters that can be calibrated from the results of in situ or laboratory tests.

3.2.1. Calibration of PM4Sand model

The PM4Sand model parameters were calibrated using both monotonic and cyclic laboratory tests on Pieve di Cento sand (BSS and GSS), as provided by Mele [25]. Notably, since experimental data are available, the critical state parameters (φ_{cv}, Q, and R) were set based on results from monotonic simple shear tests [25], while the h_{p0} parameter was calibrated using cyclic simple shear test results through the Soil Test application of PLAXIS, which study test as a soil volume element. The parameter h_{p0} was calibrated to achieve the best fit with the experimental results, in order to accurately model the liquefaction behavior of sand. In Fig. 11, the model performance for different values of h_{p0} is compared with the experimental data (CSR = 0.13) in $N_{cyc} - r_u$ (Fig. 11a) and $N_{cyc} - \varepsilon_a$ (Fig. 11b) planes. Zoomed-in views of r_u and ε_a versus N_{cyc} are also presented in Fig. 11c and d, respectively. The results show that increasing h_{p0} leads to a delayed build-up of excess pore water pressure (Fig. 11a–c) and a slower accumulation of axial strains (Fig. 11b–d). The best agreement with the experimental data is obtained for $h_{p0} = 0.52$. Although some discrepancies are observed during the initial loading cycles, the numerical and experimental results converge as liquefaction is approached.

The other secondary parameters were left with their default values. The model performance is compared with experimental results by plotting stress-strain cycles (Fig. 12a), stress paths (Fig. 12b), pore pressure ratio (Fig. 12c), and shear strains (Fig. 12d) as a function of the number of cycles (N_{cyc}). Although there are some discrepancies between the laboratory tests and the simulation, particularly before reaching liquefaction in terms of r_u and γ with N_{cyc} as already shown in Fig. 11, the model appears to accurately reproduce the soil behavior close to liquefaction. Fig. 12 compares the simulated cyclic resistance curve with the experimental data, already reported in Fig. 5a. It shows that the model is able to predict the attainment of liquefaction (see Fig. 13).

The robustness of the model calibration is further supported by the good agreement between the experimental (Fig. 5b) and simulated normalized shear modulus (G/G_0) and damping ratio increment ($D-D_0$) curves for GSS sand, as shown in Fig. 14. The numerical results were obtained using the Soil Test tool available in PLAXIS. The simulations were carried out by applying cyclic shear strain amplitudes of γ_{xy} = 0.0001 %, 0.001 %, 0.005 %, 0.01 %, 0.025 %, 0.05 %, 0.075 %, 0.1 %, and 0.2 %, under a vertical effective stress of 58 kPa, consistent with the experimental conditions. This provides additional confidence in the reliability of the PM4Sand calibration for the studied case.

The PM4Sand calibrated parameters are summarized in Table 3.

3.2.2. Calibration of Hardening Soil small strain model

HS_{ss} model has been used to model the behaviour of non-liquefiable soils such as clay and silty sand crust. The parameters have been calibrated from the results of in-situ tests (CPTU and CH) provided by Flora et al. [16] and deliverable D4.1 of LIQUEFACT project [47]. To ensure consistency with the DEEPSOIL analysis and accurately replicate the experimental shear wave velocity profile shown in Fig. 3b, the parameter m was set equal to 0.1. This choice resulted in a pseudo-constant shear stiffness with respect to the effective stresses. Consequently, G_0^{ref} was computed based on the shear wave velocity values. The corresponding reference loading-unloading modulus, E_{ur}^{ref} was calculated following the method suggested by Alpan [48], starting from the value of E_0^{ref} and assuming a ratio of E_0^{ref}/E_{ur}^{ref} equal to 5. Furthermore, the parameter E_{ur}^{ref}, which influences the shear deformation cut-off value for both stiffness decay and hysteretic damping curves, was selected to adequately simulate the experimental curves of Figs. 5b and 6d (soil C). Considering these curves, the characteristic shear strain level $\gamma_{0.7}$, at which the secant shear modulus G reduces to 70 % of the initial shear modulus G_0, has been set equal to 0.02 % for silty sand layer and 0.055 % for clayey layers. As suggested by literature [49], E_{50}^{ref} has been assumed equal to 1/3 of E_{ur}^{ref} while E_{oed}^{ref} was set equal to E_{50}^{ref}.

Friction angle is estimated from CPTU tests by using the correlation proposed by Mayne & Campanella [50]. Lastly, dilatancy angle (ψ) has been assumed equal to 10° (φ'/3) for shallowest layer (over consolidated crust) and 0 for clayey layers (OCR≈4, from CPTU).

The calibrated parameters have been summarized in Table 4.

3.3. Results and comparisons

The results achieved with fully coupled approach are presented in Fig. 15 alongside the corresponding DEEPSOIL output. The comparison reveals a strong agreement between the PLAXIS analysis—employing advanced constitutive models—and DEEPSOIL. Both simulations consistently predict the occurrence of liquefaction ($r_{u,max}$ >0.9) in the deeper GSS sand layer (4.8–6.0 m) and a linear decrease of the values of $r_{u,max}$, from 0.8 to 0.2, up to the surface of the model (Fig. 15a). The filter effect clearly observed in DEEPSOIL analysis plotting the PGA-profile is also noted in fully coupled approach (Fig. 15b), even though it results less pronounced.

Within the bottom clay layer (i.e., from 6 m to 10 m), a significant increase in PGA is observed, ranging from 0.15g to 0.24g in the DEEPSOIL simulations, and from 0.15g to 0.18g in the PLAXIS simulations. A plausible physical interpretation is that, following liquefaction, the lower 4 m of clay (from 6 m to 10 m depth) effectively behave as a dynamically isolated soil column, decoupled from the upper strata (i.e., 0 m–6 m). It is more accentuate in loosely coupled approach where

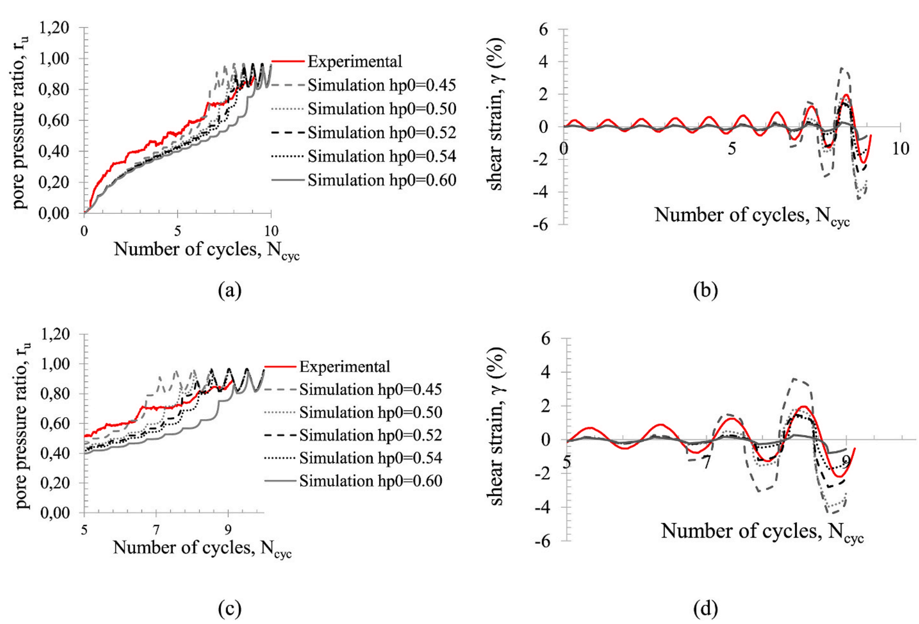

Fig. 11. Sensitivity analyses of the parameter h_{p0} in (a) $N_{cyc} - r_u$; (b) $N_{cyc} - \gamma$ planes and (c–d) zoom in the same planes.

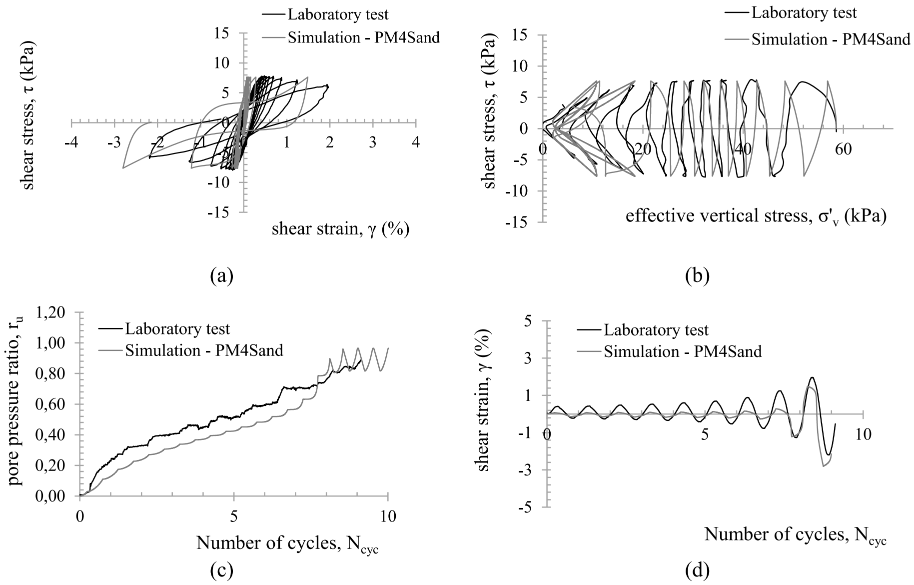

Fig. 12. Comparison between experimental data [25] and simulation of soil response with PM4Sand in (a) $\gamma - \tau$; (b) $\sigma'_v - \tau$; (c) $N_{cyc} - r_u$; (d) $N_{cyc} - \gamma$.

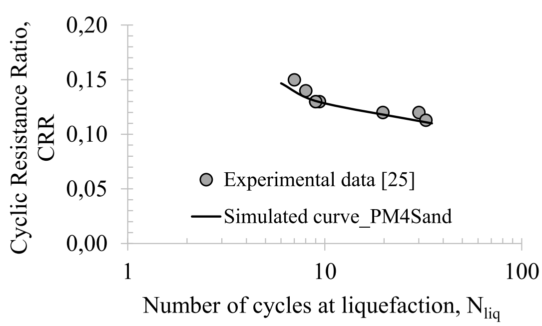

Fig. 13. Comparison between experimental data and liquefaction resistance curve simulated with PM4Sand.

Table 3
PM4Sand calibrated parameters.

Parameter	Value
D_{r0}	0.40
G_0 (kPa)	294
hp_0	0.52
Pa (kPa)	101.3
e_{max}	0.884
e_{min}	0.442
n_b	0.50
n_d	0.10
φ_{cv} (°)	38
ν	0.30
Q	7
R	0.85
Post-Shake	0

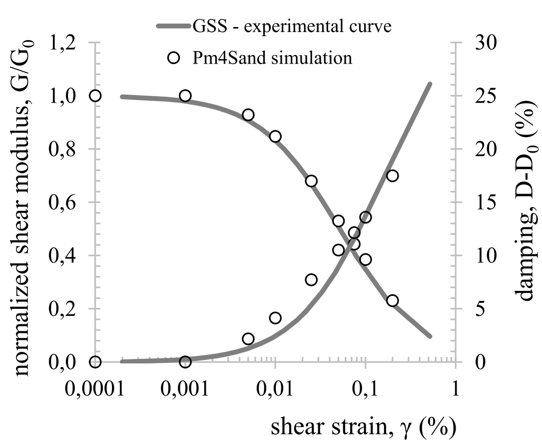

Fig. 14. Comparison between experimental data and simulated normalized shear modulus (G/G_0) and damping ratio ($D-D_0$) curves.

Table 4
HSss calibrated parameters.

	0–1.8m	4.4–4.8m	6.0–10m
Parameter	Value	Value	Value
γ	17.4	18	18
γ_{sat}	21	18	18
E_{50}^{ref} (kPa)	8269	2995	8152
E_{oed}^{ref} (kPa)	8269	2995	8152
E_{ur}^{ref} (kPa)	24807	8986	24456
ν_{ur}	0.30	0.30	0.30
m	0.1	0.1	0.1
p^{ref} (kPa)	100	100	100
G_0^{ref} (kPa)	47705	17281	47031
$\gamma_{0.7}$	0.0002	0.00055	0.00055
c' (kPa)	0	10	10
φ (°)	30	26	26
Ψ (°)	10	0	0
c'_{inc}	0	0	0

liquefied layer (4.8–6 m) experienced up to 6.2 % peak plastic shear strain against 2.6 % of fully coupled approach (Fig. 15c). Sensitivity analyses performed with loosely and fully coupled approaches (not shown for brevity) support this hypothesis, demonstrating that a model consisting solely of the 4-m-thick clay layer yields a PGA profile nearly identical to that of the full soil column. The discrepancy in peak shear strain observed between the two modelling approaches may be ascribed to the inherent differences in the representation of pore pressure–stress–strain interactions. Fully coupled formulations capture the concurrent evolution of pore pressure and mechanical response, thereby providing a more integrated simulation of soil behaviour. Conversely, loosely coupled schemes decouple pore pressure generation from the stress–strain response, which may result in a less accurate representation of soil softening. In the context of the present case study, this leads to

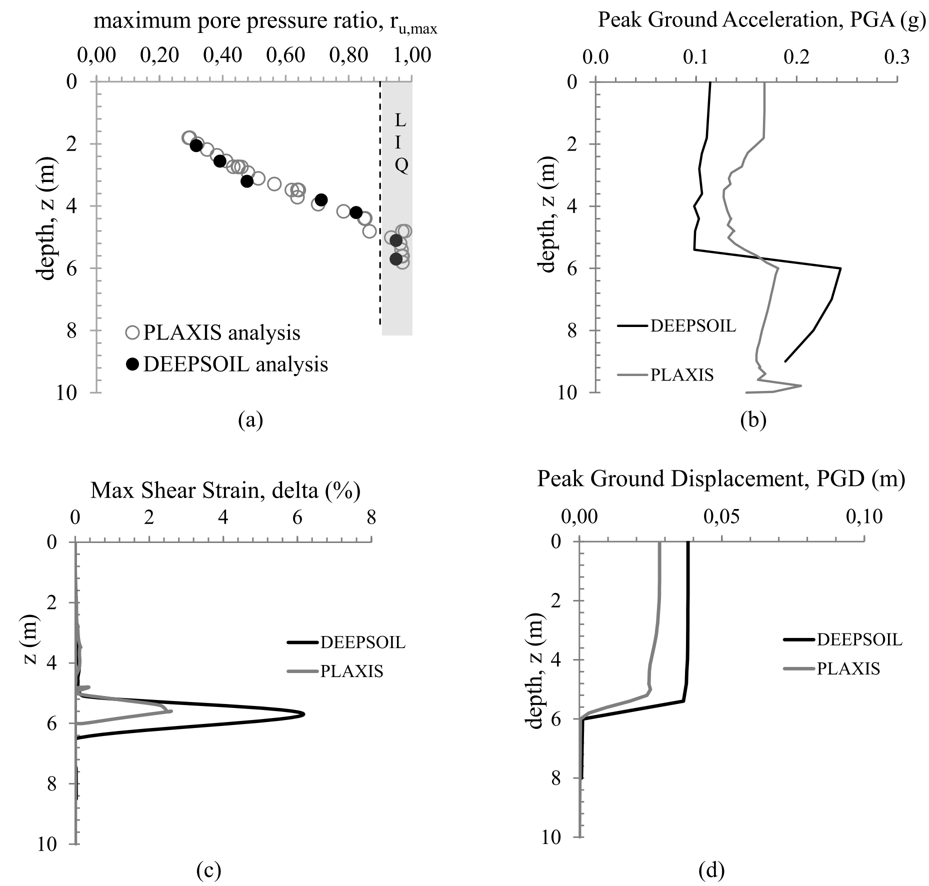

Fig. 15. (a) Comparison between estimated $r_{u,max}$ profile of Pieve di Cento site during the 2012 mainshock seismic sequence achieved with a loosely coupled (DEEPSOIL) and fully coupled (PLAXIS) approach; (b) PGA profile considering DEEPSOIL and PLAXIS analysis.

higher shear strain levels compared to those predicted by the fully coupled approach. As a consequence of the highest strain values in DEEPSOIL, a large accumulation of plastic lateral displacements is generated in the bottom sand layer reaching the value of 0.04m against 0.03 m in PLAXIS (Fig. 15d).

Fig. 16 illustrates the temporal evolution of $r_{u,max}$ at two representative depths—3.80 m and 5.10 m below ground level—corresponding to the shallow and deeper GSS layers, respectively. The results indicate a good level of agreement between the loosely coupled and fully coupled modeling approaches. However, the onset of liquefaction is observed to occur slightly earlier in the PLAXIS simulations than in those conducted with DEEPSOIL.

An additional method for detecting potential liquefaction phenomena involves analyzing significant changes in the frequency content of seismic acceleration signals, as these variations are associated with changes in soil stiffness, which are, in turn, influenced by variations in effective stress. Fig. 17 presents the Stockwell Transform [51] of the surface acceleration signals obtained from both numerical codes (DEEPSOIL and PLAXIS), allowing for time-frequency domain analysis and capturing the evolution of the signal's frequency content throughout the duration of the seismic event. As observed, once liquefaction begins to trigger (approximately 5 s after the onset of the earthquake), a significant reduction in frequency content occurs, with a shift towards lower frequencies.

4. 2D NON linear analyses

The 1D analyses presented in the previous section demonstrate that the build-up of excess pore water pressure leading to liquefaction can act as a seismic filter, abruptly reducing the acceleration transmitted to the surface (Fig. 15b). This phenomenon can have a beneficial effect on structures, as also noted by Di Ludovico et al. [11]. Indeed, empirical observations of structural damage indicate that, when liquefaction is triggered early during the seismic event, it functions as a natural

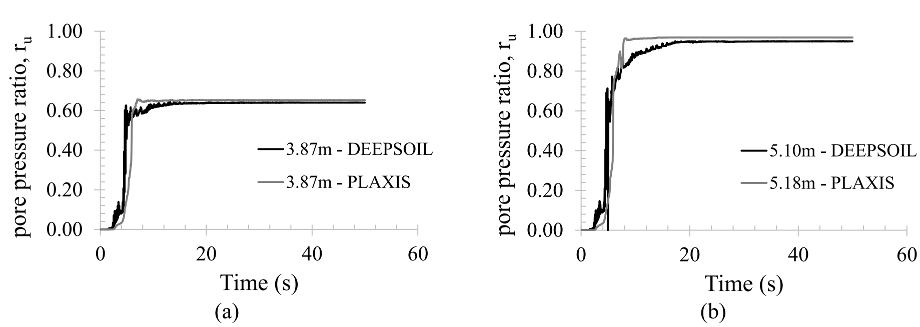

Fig. 16. Comparison of r_u-time histories computed using DEEPSOIL and PLAXIS at depths of (a) 3.87 m and (b) 5.10 m from the ground surface.

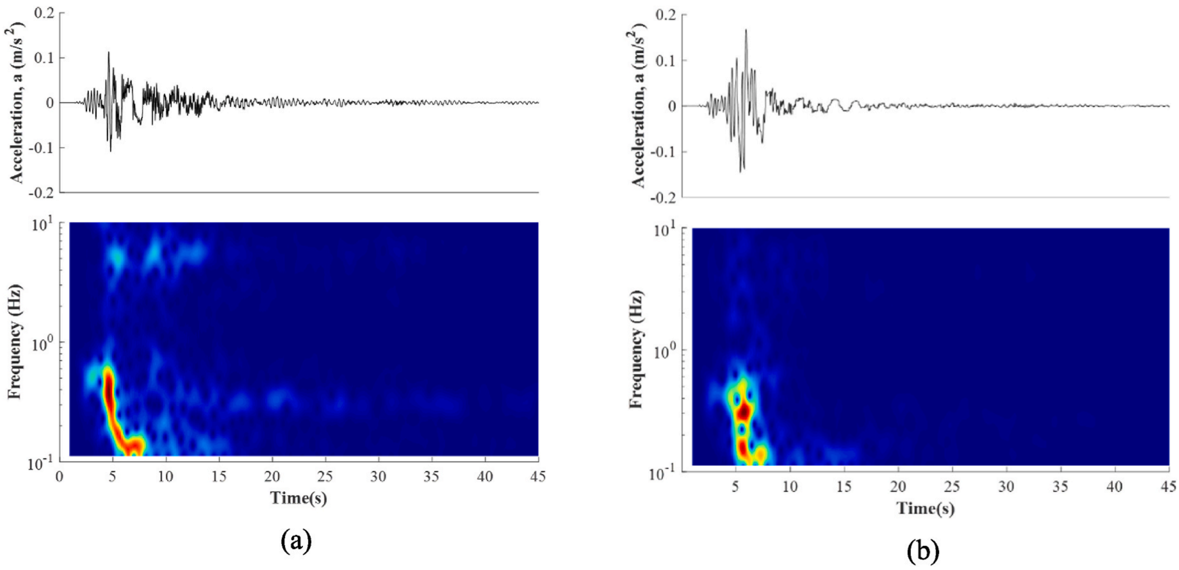

Fig. 17. Time history of surface acceleration at the Pieve di Cento site and related Stockwell transform using (a) loosely coupled approach and (b) fully coupled approach.

isolation mechanism, limiting the transmission of inertial seismic forces to the superstructure. In such cases, structural damage is primarily associated with rigid rotation or settlement. However, when liquefaction is delayed, a mixed damage pattern may occur, combining typical inertial damage (e.g., overturning of masonry walls or in-plane cracking) with localized settlements (e.g., rigid rotation or one-way diagonal cracks).

To investigate how soil-structure interaction influences the excess pore pressure ratio ($r_{u,max}$) compared to free-field conditions, a two-story masonry structure was included in the numerical model. Both

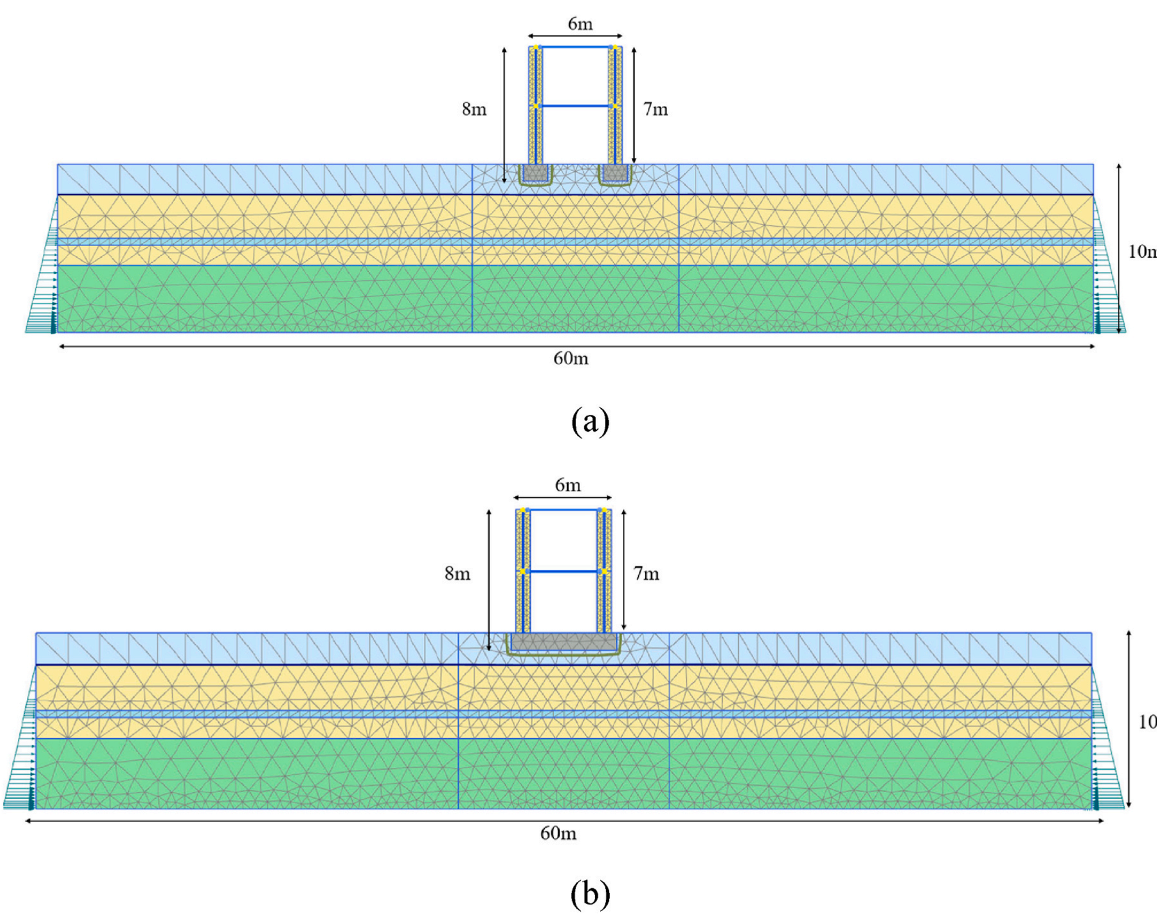

Fig. 18. (a) Finite element modelling with disconnected foundations using 2287 triangular volume elements with 15 nodes each.(b) Finite element modelling with raft foundation using 2195 triangular volume elements with 15 nodes each.

disconnected (Model A, Fig. 18a) and raft foundation (Model B, Fig. 18b) configurations were considered. The model boundaries, seismic input, and soil constitutive models are consistent with those described in Section 3.2.

As noted by Di Ludovico et al. [11], most private residential masonry buildings in the municipalities affected by the 2012 Emilia earthquake were one to three stories high, with average floor areas ranging from 70 to 100 m^2. The height, number of floors, structural load, and natural period of the modeled structure were calibrated to replicate, in a simplified manner, the characteristics of these typical masonry buildings, as they are representative of the most widespread and vulnerable building typology in the area. In particular, the structural system was modeled as a transverse section of an unreinforced masonry prototype. The floor and roof systems were represented by one-dimensional (1D) beam elements, pinned to the load-bearing walls. The masonry walls and foundations were modeled as linear elastic volume elements. This simplification is sufficient for assessing changes in excess pore pressure within the soil; however, incorporating plasticity into the structure may be essential for accurately estimating structural damage, especially when the displacement and stress demands on the masonry walls are significant [52].

Additionally, multiple interfaces, with properties derived from the surrounding soil, were included along the sides of the footings to account for potential separation or slippage between the soil and the foundation. Given the perfect symmetry of the modeled structure, no geometric or load asymmetry was incorporated, although such factors can sometimes be present in masonry structures. Since the buildings in Pieve di Cento are located approximately 500 m from the Reno River, no significant lateral spreading effects were expected [57]. Therefore, the lateral spreading phenomenon was neglected. Key properties of the modeled masonry structure are summarized in Table 5.

Fig. 19 shows the contours of the maximum pore water pressure ratio, $r_{u,max}$ (r_u computed as $1-\sigma'_v/\sigma'_{v0}$) at the end of the seismic excitation. As observed, the local increase in effective vertical stresses induced by the structural load plays a beneficial role in reducing the accumulation of excess pore water pressure. Specifically, the overall distribution of the pore water pressure ratio beneath the buildings is lower than that observed under free-field conditions. The $r_{u,max}$ values range from 0.2 to 0.7 beneath and around both the disconnected footing and the raft foundation.

The changes in the $r_{u,max}$ contours are more concentrated in Model A, where lower values (less than 0.3) are observed. In contrast, while a reduction in $r_{u,max}$ values is also seen in Model B, this effect is less pronounced than in Model A. Specifically, in Model B, the reduced $r_{u,max}$ values are concentrated near the edges of the foundation, where soil-foundation normal stresses are highest.

The difference between Model A and Model B can be attributed to the varying foundation bearing pressures, which lead to different increases in vertical effective stresses mobilized in the soil by the foundation. These stresses are greater in Model A than in Model B. The tendency of structure-induced loading to mitigate liquefaction triggering has also been observed in previous studies [53–56]. However, based on the overall distribution of $r_{u,max}$, significant settlements are still expected to occur for the modeled masonry structure.

Fig. 20a and b show the floor displacements relative to the base, or floor drifts (u_d), evaluated by subtracting from the total displacement the horizontal displacement owing to the swaying and rocking oscillation of the foundation [58].

As expected, the inter-story drifts, calculated by dividing the floor displacements by the inter-floor height, are relatively small. Specifically, they reach a maximum value of 0.21 % at the first floor and 0.09 % at the second floor for the disconnected foundation, and 0.09 % at both the first and second floors for the raft foundation. A small residual drift of 1.8 mm is observed in the case of the disconnected foundation, which results from the horizontal permanent relative movement between the footing and the first floor of the structure. This effect is entirely absent in the case of the raft foundation. The raft foundation, by providing a continuous connection between the two load-bearing walls, effectively limits both inter-story displacements and residual permanent drift.

As shown in Fig. 21, the buildings experienced considerable distortional settlements, with a permanent settlement value of 0.02 m, but no significant residual permanent global rotations. In Model A, the structure experiences notably greater transient rotations compared to Model B, due to the lower rotational stiffness of the disconnected foundation relative to the raft foundation. Based on the observed inter-story drifts and permanent vertical settlements, it can be concluded that the building exhibits a combination of inertial and liquefaction-induced damage patterns.

Table 5
Key properties of the masonry structure modeled with connected and disconnected foundations.

Parameter	Model A	Model B
Mean Foundation Bearing	~140 kPa	~80 kPa
Shallow Foundations width	1.4 m	6 m
Foundations depth and height	1 m	1 m
First Natural frequency (fixed base)	4.4 Hz	4.4 Hz
Superstructure weight (walls + floors)	275 kN/m	275 kN/m
Wall stiffness (E)	1500 MPa	1500 MPa
Wall width	0.8 m	0.8 m
Masonry wall specific weight	16 kN/m^3	16 kN/m^3
I floor and roof specific weight	10 kN/m/m	10 kN/m/m
Foundation weight	35 + 35 kN/m	150 kN/m
Base Width	6 m	6 m
Total Height superstructure	7 m	7 m

5. Conclusions

The paper aims to study the excess pore water pressure generated by the 2012 mainshock seismic sequence at the Pieve di Cento site, employing increasingly complex approaches such as loosely coupled and fully coupled models. To achieve this, the outcrop seismic signal recorded in Mirandola was deconvolved at the local bedrock and subsequently re-convoluted for the Pieve di Cento site. The seismic signal was then extrapolated, as surface motion, to a depth of 10 m during the convolution analysis. Given the stratigraphy of the soil at the Pieve di Cento site, particular emphasis was placed on modeling the top 10 m of soil using different advanced constitutive models capable of accurately calculating the accumulation of excess pore water pressure. Consistent with field observations, the numerical models implemented predict liquefaction occurrence primarily within the lower sand layer, confined above and below by clay layers. The triggering of liquefaction in a relatively deep sand layer induces the so-called *filter effect*, which can lead to a significant reduction in inertial forces and an increase in total plastic lateral displacements.

The comparison between the $r_{u,max}$ profiles obtained using loosely coupled approach (employing an energy-based excess pore pressure model) and those derived from advanced analyses demonstrate a satisfactory level of agreement. Indeed, the results presented demonstrate that, when properly calibrated, the energy-based pore pressure model implemented in DEEPSOIL can effectively predict earthquake-induced pore pressures. The simplicity of the Berrill & Davis [35] model, along with the straightforward calibration procedure based on in-situ tests proposed by Mele et al. [39], suggest that the loosely coupled approach may offer a practical and effective tool for practitioners seeking an efficient and user-friendly method for performing 1D non-linear analyses. Although, future studies will be carried out to further assess the effectiveness of the proposed method. Additionally, if feasible, an increasingly complex methodological approach can yield more accurate and reliable results, whereas the direct use of advanced constitutive models may lead to overlooked or misleading outcomes.

The results obtained from one-dimensional FEM modeling were also replicated in two-dimensional analyses, considering the presence of a

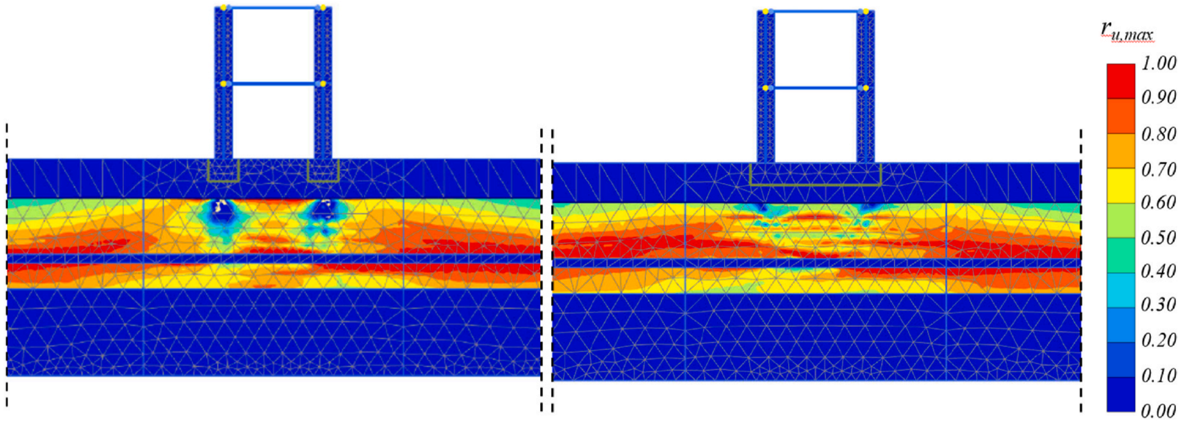

Fig. 19. Contour of pore water pressure ratio, $r_{u,max}$, during the 2012 mainshock seismic sequence with Model A (left) and Model B (right).

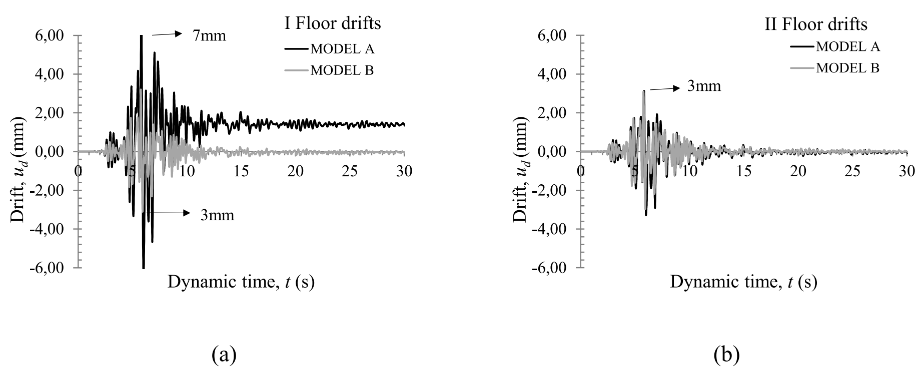

Fig. 20. (a) Structural drifts at I floor; (b) Structural drifts at II floor.

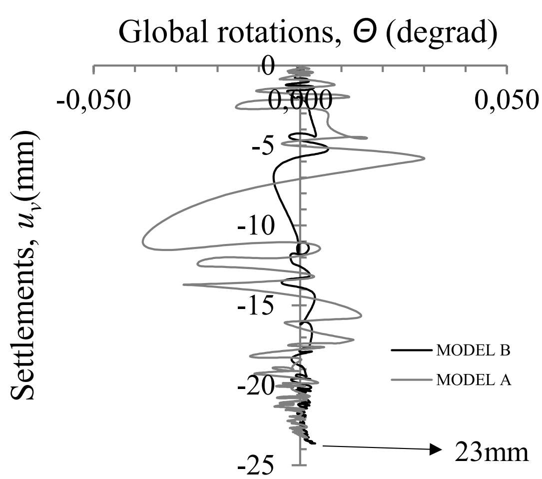

Fig. 21. Settlement-rotations behavior of masonry structure during the 2012 mainshock seismic sequence.

masonry structure with both raft and disconnected foundations. The increase in effective stresses induced by the structural load led to a consistent modification and reduction of the excess pore water pressure ratio beneath the building, as compared to free-field conditions. The magnitude of this effect varies depending on the foundation bearing pressures, which in turn cause differing increases in the vertical effective stresses mobilized in the soil by the foundation. The relatively low interstory drifts, coupled with significant distortional permanent settlements, suggest that the structural damage scenario can be attributed to a combination of reduced inertial excitations and soil vertical settlements. The differences observed relative to free-field conditions indicate that a rigorous evaluation of liquefaction susceptibility requires consideration of the actual effective stress state in the soil, especially when significant stresses are imposed by foundation loading. However, neglecting the influence of such structural loads could potentially lead to overly conservative estimates of liquefaction susceptibility.

CRediT authorship contribution statement

Lucia Mele: Writing – review & editing, Writing – original draft, Resources, Funding acquisition, Formal analysis, Data curation, Conceptualization. **Fausto Somma:** Writing – review & editing, Writing – original draft, Methodology, Formal analysis, Data curation, Conceptualization.

Declaration of competing interest

The authors declare that they have no known competing financial interests or personal relationships that could have appeared to influence the work reported in this paper.

Acknowledgements

The financial contribution of the of the following projects is gratefully acknowledged: *DPC - RELUIS project* (2024–2026), WP16: Contributi normativi – Geotecnica, Task 16.1 – Analisi della risposta sismica locale e liquefazione; *Finanziamento Ricerca di Ateneo (FRA-2022)* for the project “ASsessment of seismic Induced SettleMents and mitigAtIon Risk actions” (SISMAIR).

The authors would like to sincerely thank the anonymous reviewers for their insightful comments and suggestions, which greatly contributed to improving the quality and clarity of the paper.

Data availability

Data will be made available on request.

References

[1] Chiaradonna A. Defining the boundary conditions for seismic response analysis—a practical review of some widely-used codes. Geosciences 2022;12(2):83.

[2] Ramirez J, Barrero AR, Chen L, Dashti S, Ghofrani A, Taiebat M, Arduino P. Site response in a layered liquefiable deposit: evaluation of different numerical tools and methodologies with centrifuge experimental results. J Geotech Geoenviron Eng 2018;144(10):04018073.

[3] Tropeano G, Chiaradonna A, d'Onofrio A, Silvestri F. A numerical model for non-linear coupled analysis of the seismic response of liquefiable soils. Comput Geotech 2019;105:211–27.

[4] Fioravante V, Giretti D, Abate G, Aversa S, Boldini D, Capilleri PP, Vannucchi G. Earthquake geotechnical engineering aspects of the 2012 Emilia-Romagna earthquake (Italy). 2013.

[5] Lai CG, Bozzoni F, Mangriotis MD, Martinelli M. Soil liquefaction during the 20 may 2012 M5. 9 Emilia earthquake, northern Italy: field reconnaissance and post-event assessment. Earthq Spectra 2015;31(4):2351–73.

[6] Galli P. New empirical relationships between magnitude and distance for liquefaction. Tectonophysics 2000;324(3):169–87.

[7] Vannucchi G, Crespellani T, Facciorusso J, Ghinelli A, Madiai C, Puliti A, Renzi S. Soil liquefaction phenomena observed in recent seismic events in Emilia-Romagna Region, Italy. Ingegneria sismica 2012;2016(3):20–30.

[8] Sciarra A, Cantucci B, Buttinelli M, Galli G, Nazzari M, Pizzino L, Quattrocchi F. Soil-gas survey of liquefaction and collapsed caves during the Emilia seismic sequence. Ann Geophys 2012.

[9] Lombardi D, Bhattacharya S. Liquefaction of soil in the Emilia-Romagna region after the 2012 Northern Italy earthquake sequence. Nat Hazards 2014;73:1749–70.

[10] Manfredi G, Prota A, Verderame GM, De Luca F, Ricci P. 2012 Emilia earthquake, Italy: reinforced concrete buildings response. Bull Earthq Eng 2014;12:2275–98.

[11] Di Ludovico M, Chiaradonna A, Bilotta E, Flora A, Prota A. Empirical damage and liquefaction fragility curves from 2012 Emilia earthquake data. Earthq Spectra 2020;36(2):507–36.

[12] Tonni L, Gottardi G, Amoroso S, Bardotti R, Bonzi L, Chiaradonna A, Aversa S. Interpreting the deformation phenomena triggered by the 2012 Emilia seismic sequence on the Canale Diversivo di Burana banks. Riv Ital Geotec 2015.

[13] Minarelli L, Amoroso S, Tarabusi G, Stefani M, Pulelli G. Down-hole geophysical characterization of middle-upper quaternary sequences in the apennine foredeep, Mirabello, Italy. Ann Geophys 2016.

[14] Facciorusso J, Madiai C, Vannucchi G. CPT-based liquefaction case history from the 2012 Emilia earthquake in Italy. J Geotech Geoenviron Eng 2015;141(12): 05015002.

[15] Facciorusso J, Madiai C, Vannucchi G. The 2012 Emilia earthquake (Italy): geotechnical characterization and ground response analyses of the paleo-Reno river levees. Soil Dynam Earthq Eng 2016;86:71–88.

[16] Flora A, Bilotta E, Chiaradonna A, Lirer S, Mele L, Pingue L. A field trial to test the efficiency of induced partial saturation and horizontal drains to mitigate the susceptibility of soils to liquefaction. Bull Earthq Eng 2021;19:3835–64.

[17] Martelli L, Romani M. Microzonazione sismica e analisi della condizione limite per l'emergenza delle aree epicentrali dei terremoti della pianura emiliana di maggio-giugno 2012 (Ordinanza del commissario delegato n. 70/2012). Relazione Illustrativa 2013 (in Italian), http://ambiente.regione.emilia-romagna.it.

[18] Pingue L. DELIVERABLE D4. 3 Report on demonstration of retrofitting techniques. LIQUEFACT project; 2019. http://www.liquefact.eu/disseminations/deliverables/.

[19] Martelli L. Il progetto LIQUEFACT in emilia-romagna. Webinar proceedings 2021. https://ambiente.regione.emilia-romagna.it/it/geologia/divulgazione/pubblicazioni/atti-convegni-seminari/il-progetto-liquefactin-emilia-romagna.

[20] Paolucci E, Albarello D, D'Amico S, Lunedei E, Martelli L, Mucciarelli M, Pileggi D. A large scale ambient vibration survey in the area damaged by May–June 2012 seismic sequence in Emilia Romagna, Italy. Bull Earthq Eng 2015;13:3187–206.

[21] Huang AB, Mayne PW, editors. Geotechnical and geophysical site characterization: proceedings of the 3rd international conference on site characterization; 2008.

[22] Yusa M, Bowman ET, Cubrinovski M. Observation of microstructure of silty sand obtained from gelpush sampler and reconstituted sample. In: EPJ web of conferences, 140. EDP Sciences; 2017, 12017.

[23] ASTM D4253-06. Standard test methods for maximum index density and unit weight of soils using a vibratory table. West Conshohocken: Annual Book of ASTM Standards, ASTM International; 2006.

[24] ASTM D4254-06. Test methods for minimum index density and unit weight of soils and calculation of relative density. West Conshohocken: Annual Book of ASTM Standards, ASTM International; 2006.

[25] Mele L. Experimental study with complete stress state interpretation of undrained monotonic and cyclic simple shear tests with flexible boundaries. Acta Geotechnica 2024;19(1):147–61.

[26] Castro G. Liquefaction and cyclic mobility of saturated sands. J Geotech Geoenviron Eng 1975;101(ASCE). GT6: 551–569.

[27] JRC European Commission and Eurocode. Eurocode 8: seismic design of buildings worked examples. 2004.

[28] Chiaradonna A, Tropeano G, d'Onofrio A, Silvestri F. Interpreting the deformation phenomena of a levee damaged during the 2012 Emilia earthquake. Soil Dynam Earthq Eng 2019;124:389–98.

[29] Hashash YM, Musgrove MI, Harmon JA, Ilhan O, Xing G, Numanoglu O, Park D. In: DEEPSOIL 7.0, user manual, 7. Urbana, IL: Board of Trustees of University of Illinois at Urbana-Champaign; 2020. p. 170.

[30] Darendeli MB. Development of a new family of normalized modulus and material damping curves. the University of Texas at Austin; 2001. PhD Thesis.

[31] Chiaradonna A, Özcebe AG, Bozzoni F, Fama A, Zuccolo E, Lai CG, Silvestri F. Numerical simulation of soil liquefaction during the 20 May 2012 M6. 1 Emilia Earthquake in Northern Italy: the case study of Pieve di Cento. In: Proceedings of the 16th European conference on earthquake engineering. Thessaloniki, Grecia: 16ECEE; 2018, June. p. 18–21.

[32] Olson SM, Mei X, Hashash YM. Nonlinear site response analysis with pore-water pressure generation for liquefaction triggering evaluation. J Geotech Geoenviron Eng 2020;146(2):04019128.

[33] Biondi G, Cascone E, Di Filippo G. Affidabilita' di alcune correlazioni empiriche per la stima del numero di cicli di carico equivalente. Riv Ital Geotec 2012;46(2):9–39.

[34] Castiglia M, Santucci de Magistris F. Prediction of the number of equivalent cycles for earthquake motion. Bull Earthq Eng 2018;16(9):3571–603.

[35] Berrill JB, Davis RO. Energy dissipation and seismic liquefaction of sands: revised model. Soils Found 1985;25(2):106–18.

[36] Green RA, Mitchell JK, Polito CP. An energy-based excess pore pressure generation model for cohesionless soils. In: Proceedings of the John Booker memorial symposium, Sidney Australia. Rotterdam, Netherlands: AA Balkema Publishers; 2000.

[37] Tomasello G, Porcino DD. Energy-based pore pressure generation models in silty sands under earthquake loading. Geosciences 2024;14(6):166.

[38] Mele L, Flora A. On the prediction of liquefaction resistance of unsaturated sands. Soil Dynam Earthq Eng 2019;125:105689.

[39] Mele L, Lirer S, Flora A. A simple procedure to calibrate a pore pressure energy-based model from in situ tests. Acta Geotechnica 2023;18(3):1569–91.

[40] Boulanger RW, Idriss IM. CPT and SPT liquefaction triggering procedures. Davis, California, USA: University of California at; 2014. Report No UCD/GCM-14/01.

[41] Kwok AOL, Stewart JP, Hashash YMA, Matasovic N, Pyke R, Wang Z, Yang Z. Use of exact solutions of wave propagation problems to guide implementation of nonlinear seismic ground response analysis procedures. J Geotech Geoenviron Eng 2007;133:1385–98.

[42] Boulanger RW, Ziotopoulou AK. PM4Sand (Version 3): a sand plasticity model for earthquake engineering applications. Davis, Calif: Center for Geotechnical Modeling Report No. UCD/CGM-15/01, Department of Civil and Environmental Engineering, University of California; 2015.

[43] Dafalias YF, Manzari MT. Simple plasticity sand model accounting for fabric change effects. J Eng Mech 2004;130(6):622–34. ASCE.

[44] Boulanger RW. High overburden stress effects in liquefaction analyses. J Geotechn Geoenviron Eng., ASCE 2003;129(12):1071–82.

[45] Bolton MD. The strength and dilatancy of sands. Geotechnique 1986;36(1):65–78.

[46] Schanz T, Vermeer P, Bonier P. Formulation and verification of the hardening soil model. In: Beyond 2000 in computational geotechnics. Rotterdam: Balkema; 1999.

[47] LIQUEFACT deliverable 4.1. Report on the comparison of soil response before and after ground treatment at the pilot site. http://www.liquefact.eu/disseminations/deliverables/; 2020.

[48] Alpan I. The geotechnical properties of soils. Earth Sci Rev 1970;6:5–49.

[49] Obrzud RF, Truty A. The hardening soil model -a practical guidebook. Z Soil.PC 100701 report revised 21.10.2018 2018.

[50] Mayne PW, Campanella RG. Versatile site characterization by seismic piezocone. In: Proceedings of the 16th international conference on soil mechanics and geotechnical engineering. IOS Press; 2005. p. 721–4.

[51] Stockwell RG, Mansinha L, Lowe RP. Localization of the complex spectrum: the S transform. IEEE Trans Signal Process 1996;44(4):998–1001.

[52] Somma F, Lignola G, Ramaglia G, et al. An interdisciplinary investigation of the seismic performance of a historic tower in Istanbul during the 1999 Kocaeli earthquake. Bull Earthquake Eng 2023;21:2921–45. https://doi.org/10.1007/s10518-023-01638-6.

[53] Karamitros DK, Bouckovalas GD, Chaloulos YK. Seismic settlements of shallow foundations on liquefiable soil with a clay crust. Soil Dynam Earthq Eng 2013;46: 46–76.

[54] Dashti S, Bray JD. Numerical simulation of building response on liquefiable sand. J Geotech Geoenviron Eng 2013;139(8):1235–49.

[55] Bertalot D, Brennan AJ. Influence of initial stress distribution on liquefaction-induced settlement of shallow foundations. Geotechnique 2015;65(5):418–28.

[56] Flora A, Elia S, Valtucci F, Lirer S. Simplified prediction of settlements of shallow foundations caused by earthquake-induced excess pore water pressures. Soil Dynam Earthq Eng 2025;194:109383.

[57] Somma F, Millen M, Bilotta E, Flora A, Viana Da Fonseca A. Vulnerability assessment of RC buildings to lateral spreading. Bull Earthq Eng 2020;18:3629–57.

[58] Somma F, Bilotta E, Flora A, Viggiani GM. Centrifuge modeling of shallow foundation lateral disconnection to reduce seismic vulnerability. J Geotech Geoenviron Eng 2022;148(2):04021187.